



Comparisons between homogeneous boundaries and heterophase interfaces in plastic deformation: Nanostructured Cu micropillars vs. nanolayered Cu-based micropillars

J.Y. Zhang, G. Liu*, J. Sun*

State Key Laboratory for Mechanical Behavior of Materials, Xi'an Jiaotong University, Xi'an 710049, People's Republic of China

Received 25 March 2013; received in revised form 28 July 2013; accepted 30 July 2013

Available online 24 August 2013

Abstract

Both the homogeneous boundaries and the heterophase interfaces play important roles in crystalline plasticity as they often serve as obstacles for dislocation motion, as well as dislocation sources/sinks. In this work, microcompression tests were carefully performed to explicitly identify the relevant plasticity mechanisms of nanostructured micropillars with five distinct nanostructures: (i) Cu nanotwinned multicrystalline micropillars; (ii) Cu nanocrystalline multicrystalline micropillars; (iii) Cu/X (X = Cr, Zr) nanotwinned nanolayered micropillars; (iv) Cu/X nanocrystalline nanolayered micropillars; and (v) Cu/Cu–Zr crystalline/amorphous nanolayered micropillars. By characterizing their stress–strain response and evolution of strain-rate sensitivity (SRS) with strain, our findings elucidate the effects of homogeneous boundaries, heterophase interfaces and their coupling effects on the plastic yield, and reveal the fundamentally different roles these perform in the rate-limiting process of nanomaterials. In sharp contrast to the normal strain-dependent SRS in nanostructured Cu micropillars with homogeneous boundaries that monotonically decreases with increasing strain, nanolayered Cu-based micropillars with heterophase interfaces exhibit inverse strain-dependent SRS that monotonically increases with increasing strain. These expected (normal) and unexpected (inverse) SRSs are quantitatively explained by a dislocation model in terms of the strain-related dislocation mean free path. These findings provide valuable insights into our understanding of the fundamental roles that homogeneous boundaries and heterophase interfaces play in plastic deformation.

© 2013 Acta Materialia Inc. Published by Elsevier Ltd. All rights reserved.

Keywords: Nanostructures; Homogeneous boundary; Heterophase interface; Strain-rate sensitivity; Size effects

1. Introduction

Nanomaterials, e.g. nanocrystalline (NC) metals, nanotwinned (NT) metals and nanolayered (NL) films, offer outstanding mechanical properties compared to their bulk counterparts making them suitable for engineering applications [1,2]. These outstanding properties are due to the homogeneous boundaries (e.g. grain boundaries (GBs) and twin boundaries (TBs))/heterophase interfaces (e.g. crystalline/crystalline interfaces (CCIs) and crystal-

line/amorphous interfaces, (CAIs)) and nanoscale effects associated with the structural peculiarities of nanostructured materials, where the volume fraction of the GBs/interfaces is extremely high, and the intrinsic size (D , including grain size d , twin thickness λ , and layer thickness h) does not exceed 100 nm [3,4]. Manipulation of internal feature size to control mechanical properties is standard practice among material scientists and engineers, since the plastic characteristics of nanomaterials are highly sensitive to their microstructural features [1–6]. Before these nanomaterials can be used, it is crucial to understand the roles that homogeneous boundaries/heterophase interfaces play in plastic flow in light of the plasticity micromechanisms involved.

* Corresponding authors. Tel.: +86 (0)2982668695; fax: +86 (0)2982663453.

E-mail addresses: lgammer@mail.xjtu.edu.cn (G. Liu), junsun@mail.xjtu.edu.cn (J. Sun).

It is well known that creating microstructures (e.g. GBs, TBs, precipitates, dislocation forests or solute atoms) that hinder dislocation motion results in a significant increase in the strengths of crystalline materials, because plasticity depends sensitively on dislocation dynamics [1–6]. Grain refinement is a suite of metallurgical techniques used to implement GB strengthening. The GB strengthening of materials is usually well captured by the Hall–Petch relation [7]. In GB strengthening, the GBs act as pinning points and impede further dislocation propagation. As the internal size d shrinks to the nanoregime, the density of dislocation sources within a grain becomes too low to accommodate the imposed deformation, leading to mechanical strengthening [8–10]. This dislocation-starved state implies that the deformation mechanism must change from dislocation migration-limited plasticity to some other mechanism such as dislocation nucleation-limited plasticity [8,9,11,12]. Along with super-strength, high strain-rate sensitivity (SRS, m) emerges in NC (non-twinned) metals, such as Cu [13], Ni [14], Al [15] and Au [16], potentially due to more dislocation–GB interactions. One viable route to illustrate this complexity is to investigate the size-driven strengths [17–20] and ultrahigh SRS [21,22] of single-crystal micro/nanopillars, both of which monotonically increase with reduction in size D . Currently, the micro-mechanism of the size-dependent plastic characteristics of micron- and submicron-sized single-crystal pillars is believed to stem from the multiplication of dislocations caused by the activation of internal dislocation sources [21,23–26]. In contrast, nanosized pillars are starved of mobile dislocations and therefore the creation of dislocations from limited internal sources is required to sustain their plastic deformation [8,9,12,26]. One kinetic signature of the shift in deformation mechanisms is the reduction in activation volume (V^*) to as little as $1\text{--}10b^3$ for boundary sources as opposed to $100\text{--}1000b^3$ for Frank–Read-type bulk sources [26].

In random-oriented NT materials, the coexistence of TBs and GBs makes the plastic deformation even more

complicated [27]. Although embedding nanotwins into the matrix can significantly enhance the strengths and the SRS of nanomaterials [28–31] in a similar way to that of GBs, the role TBs play in other extraordinary behaviors, e.g. substantial strain hardening [32,33], detwinning [34] and abnormal grain growth [35], are still highly active research topics. Most recently, to determine the origins of the surprising mechanical properties of NT materials, Jang et al. [30] fabricated arrays of vertically aligned single-crystal NT Cu nanopillars. They reported that a brittle-to-ductile transition occurs in samples with orthogonally oriented TBs, and shear offsets and significant detwinning are the dominant mechanisms in slanted TB samples [30]. Zhang et al. [36–38] have prepared NT multilayers and have shown that the NTs can significantly delay the onset of softening and enhance the mechanical strength of these materials.

In parallel, NL materials are attractive in many applications because they simultaneously manifest high strength and high ductility [39–42], properties that are usually thought to be mutually exclusive. Much work has been carried out in the past 15 years to ascertain the scaling laws between layer thickness and mechanical properties [36–38,43–48]. However, the exploitation of the full potential of NLs requires a better understanding of the effects of heterophase interfaces on plastic characteristics. Unfortunately, the complicated interactions within NL systems obscure the individual role of each microstructural feature.

In this work, to elucidate the specific role(s) that a particular boundary plays in plastic deformation, we investigate the SRS of five samples with distinct internal features: (i) NT Cu multicrystalline micropillars (NTs); (ii) NC Cu multicrystalline micropillars (NCs); (iii) Cu/X ($X = \text{Cr}, \text{Zr}$) NT–NL micropillars (NTNLs); (iv) Cu/X NC–NL micropillars (NCNLs); and (v) Cu/Cu–Zr crystalline/amorphous NL micropillars (C/ANLs), as schematically shown in Fig. 1. We attempt to identify the most important structural features governing the plastic characteristics of these materials and to reveal the underlying mechanisms.

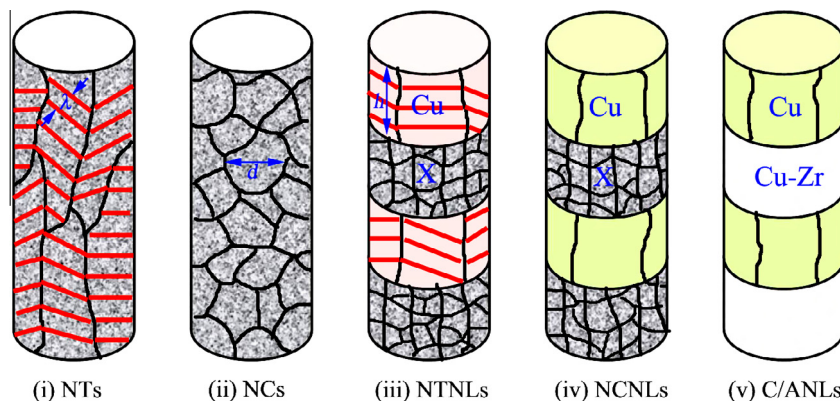


Fig. 1. Schematic illustrations of (i) Cu nanotwinned multicrystalline micropillars (NTs); (ii) Cu nanocrystalline multicrystalline micropillars (NCs); (iii) Cu/X ($X = \text{Cr}, \text{Zr}$) nanotwinned nanolayered micropillars (NTNLs); (iv) Cu/X nanocrystalline nanolayered micropillars (NCNLs); and (v) Cu/Cu–Zr crystalline/amorphous nanolayered micropillars (C/ANLs).

2. Experimental procedures

2.1. Sample preparation and microstructure characterization

The Si-supported $\sim 2 \mu\text{m}$ thick nanoscaled crystalline/amorphous Cu/Cu–Zr multilayers with $h = 100 \text{ nm}$ and crystalline/crystalline Cu/X ($X = \text{Cr, Zr}$) multilayers with $h = 125 \text{ nm}$ were prepared by using direct current (DC) magnetron sputtering at room temperature. To tailor the internal structure of the Cu/X multilayers, two different deposition rates (1.0 and 0.2 nm s^{-1}) were chosen for the Cu layers, while the deposition rates for the X layers were a constant $\sim 0.5 \text{ nm s}^{-1}$. The X layer was initially deposited on the substrate and the cap layer of the multilayer was Cu. For comparison purposes, the $\sim 1.6 \mu\text{m}$ thick NT Cu films and NC Cu films were also prepared. The chamber was evacuated to a base pressure of $\sim 6.0 \times 10^{-8}$ torr, and $1.0\text{--}2.5 \times 10^{-3}$ torr Ar were used during deposition. The target purities of Cu, Cr and Zr were 99.99%, 99.95% and 99.95%, respectively. The substrate was neither heated nor cooled during deposition. X-ray diffraction (XRD) was carried out using a Rigaku D/max-RB X-ray diffractometer with Cu K_α radiation and a graphite monochromator. Transmission electron microscopy (TEM) observations of the micro- and nanostructural features in all specimens were performed using a JEOL-2100 high-resolution electron microscope operating at 200 kV.

2.2. Fabrication of nanolayered micropillars and nanostructured Cu micropillars

The Cu-based NL micropillars with interface planes perpendicular to the cylinder axis as well as the Cu NTs and NCs were fabricated from the as-deposited films using a Helios Nano Lab 600i dual-beam focused ion beam (FIB) system, which also allows scanning electron microscopy (SEM) observations. The diameter of the micropillars was chosen to be $\sim 550 \pm 25 \text{ nm}$ to restrict the height-to-diameter ratio ~ 3 in order to avoid buckling of the sample during compression, as schematically shown in Fig. 1. Note that due to the limited thickness of the as-deposited films, only the top of the machined pillars is composed of metallic films, while the base consists of the substrate material (Si). In order to minimize the potential ion irradiation damage due to Ga ion beam and to clean any redeposited materials from the pillar surface, the final step of FIB milling was performed under a reduced voltage (15 kV) and current (15 pA). Note too that we did not apply a protective coating layer in order to avoid any contribution to the mechanical response from foreign layers. The dimensions of the micropillars and the taper were measured by SEM. The taper angles (ψ) of the pillars found to be between 2° and 4° .

2.3. Flat punch compression test

The microcompression test was performed on a Hysitron Ti 950 with a $10 \mu\text{m}$ side-flat quadrilateral

cross-section diamond indenter. The tip–pillar alignment was undertaken with the aid of an optical microscope. All the micropillars were compressed under strain-rate-controlled mode up to strains (ϵ) $\sim 15\text{--}30\%$, followed by a holding segment of 5 s prior to unloading. The strain rates ($\dot{\epsilon}$) ranged from 2×10^{-4} to $2 \times 10^{-3} \text{ s}^{-1}$. To improve the reliability and accuracy of the present measurements, great efforts were devoted to the correction of thermal drift in the microcompression test. In the present study, the allowable drift rate was set at 0.01 nm s^{-1} , which is 10-fold smaller than the typical value (0.1 nm s^{-1}) used in nanoindentation compression tests. Therefore, in the present mechanical tests, the effect of thermal drift could be neglected. Force–displacement data were continuously recorded, and the initial geometry of the pillar was measured from the SEM images. True stress–strain curves were calculated using a constant volume, homogeneous deformation assumption model to characterize the deformation behavior [49–51]. After considering the effects of substrate and tapers, the true strain ϵ_T and true stress σ_T are expressed as:

$$\begin{aligned} \epsilon_T &= \frac{1}{E_p} \frac{PL_p}{A_0L_0} + \ln \left(\frac{L_0}{L_p} \right) \\ &= \frac{1 + \frac{L_0}{r_0} \tan \psi}{E_{\text{measured}}} \frac{PL_p}{A_0L_0} + \ln \left(\frac{L_0}{L_p} \right), \end{aligned} \quad (1)$$

and

$$\begin{aligned} \sigma_T &= \frac{P}{A_p} = \frac{PL_p}{A_0L_0} \\ &= \frac{P}{A_0L_0} \left\{ L_0 - \left[u_{\text{tot}} - \frac{PL_{\text{Si}}}{E_{\text{Si}}A_{\text{Si}}} - \frac{\sqrt{\pi}P(1 - \nu_m^2)}{2E_{\text{Si}}\sqrt{A_{\text{Si}}}} \right] \right\}, \end{aligned} \quad (2)$$

where A_0 is the cross-sectional area at half the initial height (L_0) of the pillar; r_0 is the radius at the top of the pillar; L_p and A_p are the final height and average cross-sectional area, respectively; P is the load; E_p is the true modulus of the tested micropillars without tapers and E_{measured} is the measured modulus of the tapered micropillars from the unloading curves; u_{tot} is the total displacement; ν_m is the Poisson's ratio of the micropillars (~ 0.33); A_{Si} , L_{Si} and E_{Si} are respectively the average cross-sectional area, the total length and the modulus of the substrate Si pillar.

3. Experimental results

3.1. Microstructure of Cu nanostructures and Cu-based NL micropillars

On the basis of the internal features in the multilayers, the NL micropillars were classified into Cu/X ($X = \text{Cr, Zr}$) NTNLs, Cu/X NCNLs and Cu/Cu–Zr C/ANLs. Typical cross-sectional TEM images of the NL samples are displayed in Fig. 2a–e. It is clearly found that the Cu layers have $\sim 40 \pm 15 \text{ nm}$ columnar grains and the X layers have $\sim 15 \pm 5 \text{ nm}$ grains. The average grain size of Cu (d_{Cu})

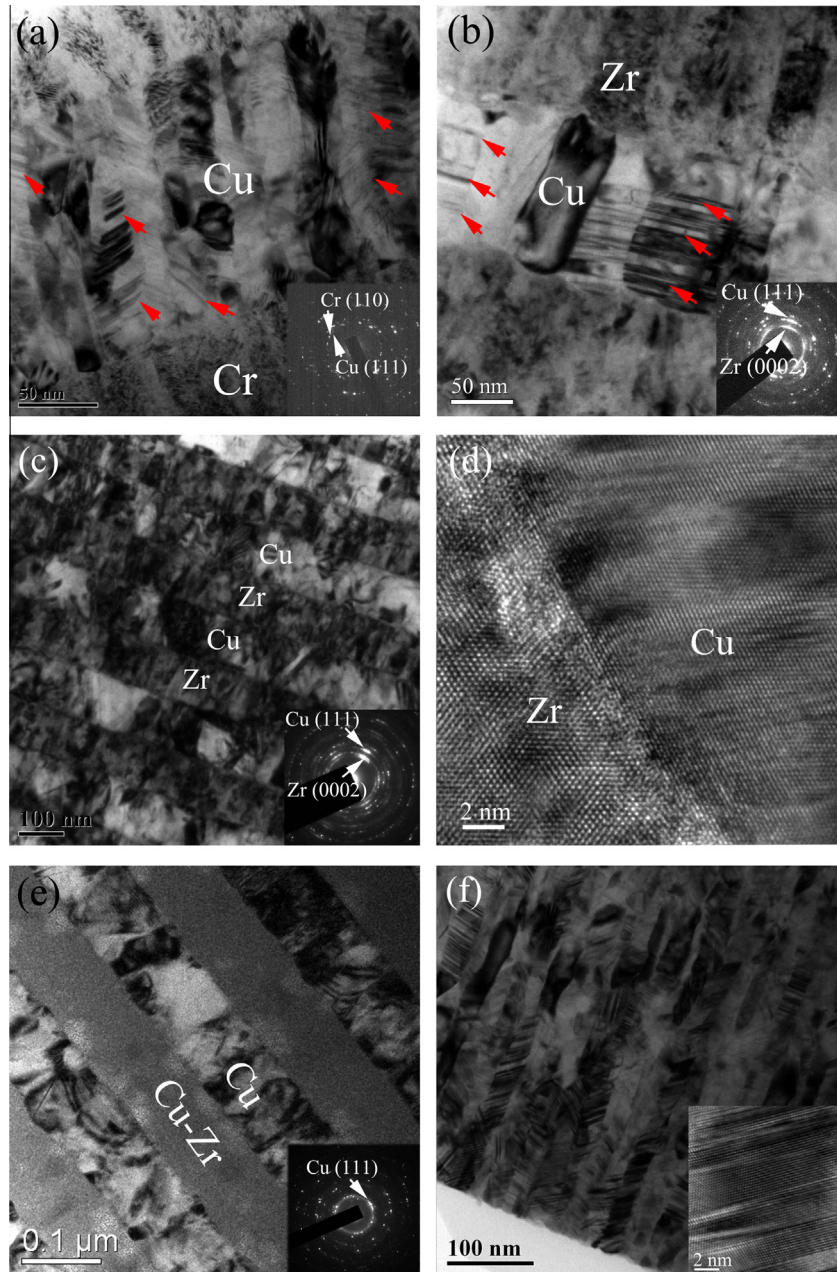


Fig. 2. Typical TEM micrographs of (a) Cu/Cr NTNLs, (b) Cu/Zr NTNLs, (c) Cu/Zr NCNLs, (d) interfacial structure of Cu/Zr NCNLs, (e) Cu/Cu–Zr C/ANPs and (f) Cu NTs. Insets are the corresponding selected-area diffraction patterns and high-resolution TEM images of nanotwins, respectively.

scales with h , while that of X (d_X) is almost independent of h . Abundant dislocations are observed within the constituent layers and at the heterophase interfaces. In all the nanolayers, the interfaces are distinguishable without significant intermixing. The selected-area diffraction patterns also show strong Cu (111), Cr (100) and Zr (0002) textures and amorphous nature in glassy Cu–Zr layers in multilayers, consistent with the XRD patterns. Careful microstructure examinations give a number fraction of nanotwins in Cu layers of about $\sim 75\%$ in Cu/Cr NTNLs and $\sim 48\%$ in Cu/Zr NTNLs, both of which show an almost identical twin thickness $\lambda \approx 8$ nm. More details

about the internal features of the multilayers can be found in our previous work for Cu/ X [39,48] and Cu/Cu–Zr [46,52].

XRD results reveal that the NT Cu films show a strong (111) peak, while the NC Cu films exhibit a polycrystalline nanostructure with random orientations. The cross-sectional TEM micrographs of the Cu NTs show that nanotwins have an average thickness $\lambda \approx 8 \pm 3$ nm, as seen in Fig. 1f. In contrast, TEM observations show that the Cu NCs have nanosized $d \approx 110 \pm 30$ nm grains. Some dislocations and planar defects are observed in the grain interiors.

3.2. Mechanical response of Cu nanostructures

The representative true stress–strain curves of the Cu NTs compressed at different strain rates are shown in Fig. 3a. It is noticeable that the true stress–strain curves show a smooth transition from elastic to plastic deformation until the maximum strength is reached (at strain $\varepsilon \approx 0.06$), after which the Cu NTs first soften sharply and then harden slowly, accompanied by some sudden stress drops. Unlike the Cu NTs, the Cu NCs exhibit relatively smoother plastic flow without any sharp stress drops. In addition, only the hardening-to-softening behavior is observed in the Cu NCs, as shown in Fig. 3b. A comparison of Fig. 3a with b for Cu NTs and Cu NCs shows that there clearly exists a rate-dependent deformation behavior of both nanostructured Cu pillars, i.e. a faster rate leads to a higher flow stress at a plastic strain (ε_p) < 8%. Due to dislocation storage and interactions, the plastic mechanisms generally evolve with ε_p in face-centered cubic (fcc) polycrystalline samples [53] as well as in bulk fcc single crystals [54]; we thus plot the strengths $\sigma_{0.5}$ (at $\varepsilon_p = 0.5\%$), σ_1 (at $\varepsilon_p = 1\%$), $\sigma_{2.5}$ (at $\varepsilon_p = 2.5\%$) and $\sigma_{3.5}$ (at $\varepsilon_p = 3.5\%$) against $\dot{\varepsilon}$, as shown in Fig. 3c. It is found that the strengths monotonically increase with increasing $\dot{\varepsilon}$. A similar phenomenon is observed in the Cu NCs (see Fig. 3d).

3.3. Mechanical response of Cu-based NL micropillars

Fig. 4a–c presents the typical true stress–strain curves of $h = 125$ nm Cu/Cr NTNLs and NCNLs and $h = 100$ nm Cu/Cu–Zr C/ANLs, respectively, at different strain rates.

All of the true stress–strain curves exhibit a nearly linear elastic behavior until the initial yield point (σ_0) is reached ($\varepsilon \approx 0.03$) followed by inelastic deformation. It appears that a faster rate results in a higher flow stress, indicative of a marked $\dot{\varepsilon}$ -effect. Furthermore, it is noticeable that, at low $\dot{\varepsilon}$, all of the compressive curves transition from initial hardening stage to softening stage. Nevertheless, only the strain hardening was observed in the two types of the fastest compressed Cu/Cr pillars within the studied strain range $\leq 20\%$. Interestingly, it is found that a faster rate delays the softening to a greater strain. A comparison of Fig. 4a and b indicates that the existence of nanotwins indeed enhances the strengths of the samples. Similar results are found in the Cu/Zr NTNLs and NCNLs, respectively. It is intriguing to find that no sharp stress drops are observed in the compressive curves of C/ANLs (see Fig. 4c), implying that the shear banding events often associated with monolithic metallic glasses are completely suppressed. Likewise, the $\dot{\varepsilon}$ -dependent strengths at different strains are displayed in Fig. 4d for Cu/X NTNLs, in Fig. 4e for Cu/X NCNLs and in Fig. 4f for Cu/Cu–Zr C/ANLs, respectively. It nevertheless appears that the strengths monotonically increase with increasing $\dot{\varepsilon}$ for all the NL materials.

3.4. SRS of Cu nanostructures and Cu-based NL micropillars

It is well established that the thermally activated mechanisms contributing to plastic deformation processes in metals are often quantitatively interpreted by examining

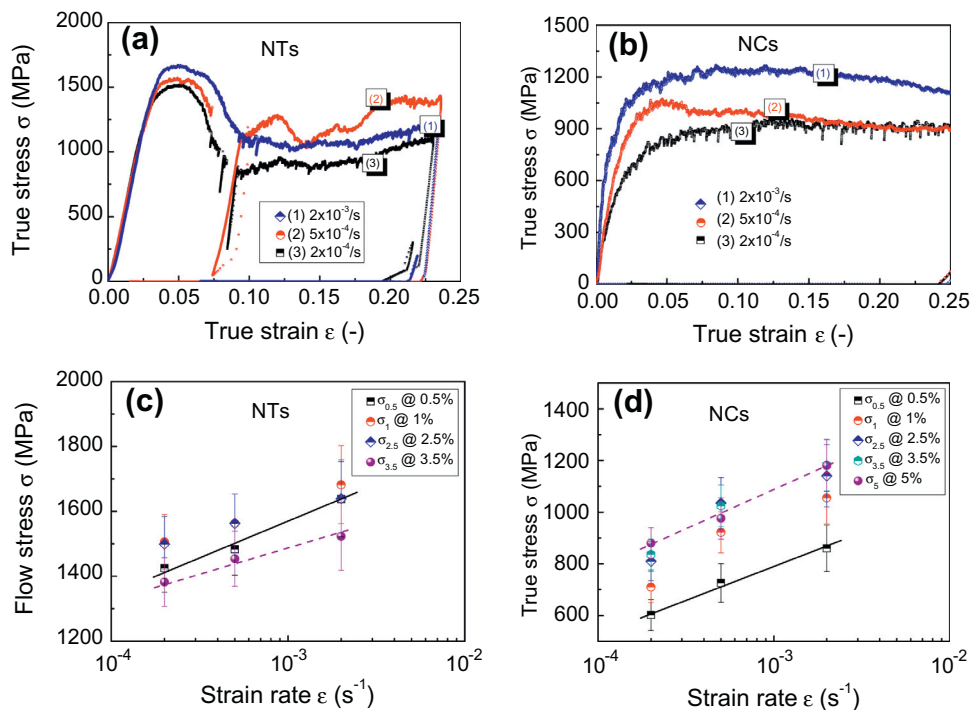


Fig. 3. Representative true stress–strain curves of (a) Cu NTs and (b) Cu NCs. The strengths at different strains as a function of strain rates for (c) Cu NTs and (d) Cu NCs.

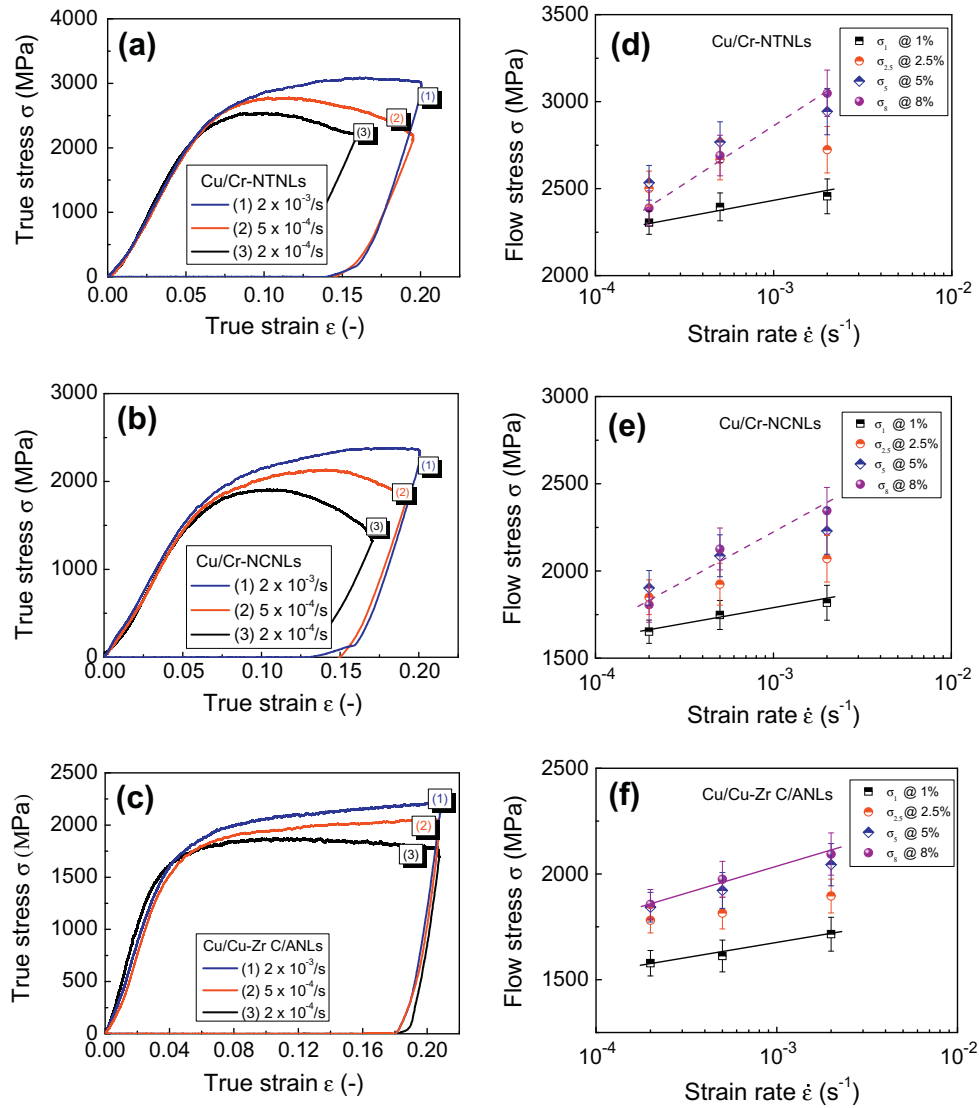


Fig. 4. Representative true stress–strain curves of (a) Cu/Cr NTNLs, (b) Cu/Cr NCNLs and (c) Cu/Cu–Zr C/ANLs at different strain rates. The strengths at different strains as a function of strain rates for (d) Cu/Cr NTNLs, (e) Cu/Cr NCNLs and (f) Cu/Cu–Zr C/ANLs.

the SRS index, m , and the activation volume, V^* . The non-dimensional SRS is defined as [26,55]:

$$m = \frac{\sqrt{3}k_B T}{V^* \sigma} = \frac{\partial \ln(\sigma)}{\partial \ln(\dot{\epsilon})}, \quad (3)$$

where σ is the stress, T is the absolute temperature and k_B is the Boltzmann constant.

The SRS m as a function of ϵ_p obtained from Figs. 3 and 4 is plotted in Fig. 5a for Cu nanostructures and in Fig. 5b for Cu-based NL micropillars, and can be compared with those of NT Cu [56] and NL Cu/Ni [57] reported before. It is found that the Cu nanostructures show monotonically reduced SRS with increasing ϵ_p , consistent with the NT Cu [56]. The SRS m of Cu NCs is far greater than that of $d = 100$ nm bulk Cu ($m \approx 0.02$), while the SRS m of Cu NTs almost equals that of $\lambda = 15$ nm bulk Cu within the scatter, but is still greater than that of $\lambda = 100$ nm

macroscopic samples ($m \approx 0.02$). Unexpectedly, the SRS m of NL systems monotonically increases with increasing ϵ_p , similarly to that of Cu/Ni pillars [57]. Interestingly, it appears that the SRS m is the largest for the Cu/Zr NCNLs, then the Cu/Cr NCNLs, followed by the Cu/Cu–Zr C/ANLs. Additionally, these SRS m values of Cu nanostructures and Cu-based NL micropillars are much greater than that of bulk Cu ($m \approx 0.006$).

It is well accepted that the SRS m is inversely proportional to the activation volume (V^*), which can be considered as a signature of deformation mechanisms in general, and dislocation processes in particular [26]. To gain deeper insights into the dislocation activities and the potential hardening/softening mechanisms, V^* as a function of ϵ_p is plotted in Fig. 6a for nanostructured Cu pillars and in Fig. 6b for NL pillars. It is found that for NT and NC Cu pillars (Fig. 6a), V^* generally increases with smaller

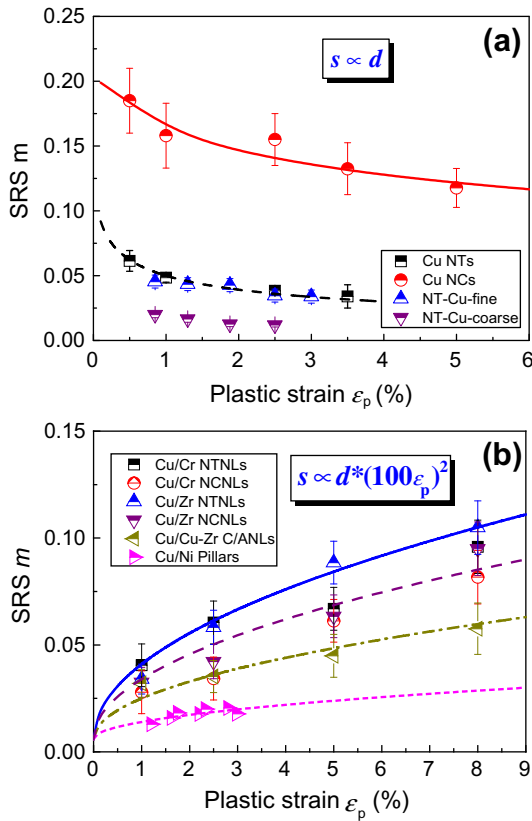


Fig. 5. The SRS m as a function of plastic strain for (a) Cu nanostructures, including Cu NTs, Cu NCs, nanotwinned Cu with fine and coarse nanotwins [56]; and (b) Cu-based nanolayered pillars, including Cu/X ($X = \text{Cr}, \text{Zr}$) NTNLs, Cu/X NCNLs, Cu/Cu–Zr C/ANLs and Cu/Ni micropillars [57]. The fitting curves in (a) and (b) are obtained from Eq. (9b) by using $s \propto d$ and $s \propto d \cdot (100 \cdot \varepsilon_p)^2$, respectively.

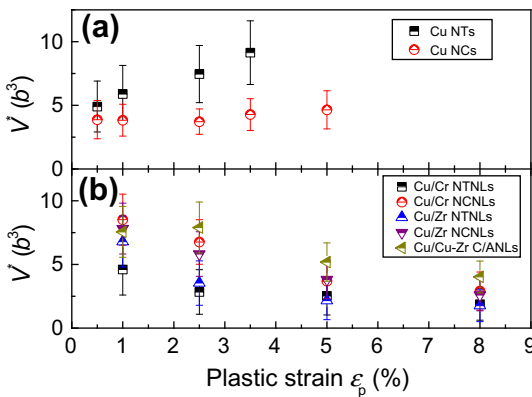


Fig. 6. The activation volume V^* as a function of plastic strain ε_p for (a) Cu nanostructures, including Cu NTs and NCs; and (b) Cu-based nanolayered pillars, including Cu/X ($X = \text{Cr}, \text{Zr}$) NTNLs, Cu/X NCNLs and Cu/Cu–Zr C/ANLs.

ε_p , in sharp contrast with that of NL samples, showing a monotonic reduction of V^* with increasing ε_p (Fig. 6b). Furthermore, the values of V^* for both nanostructured Cu pillars and Cu-based NL pillars are extremely small ($V^* < 10b^3$).

3.5. Deformation morphologies of Cu nanostructures and Cu-based NL micropillars

Fig. 7a–f and their insets present SEM images of (a) Cu NTs, (b) Cu NCs, (c) Cu/Cr NTNLs, (d) Cu/Cr NCNLs, (e) Cu/Zr NCNLs and (f) Cu/Cu–Zr C/ANLs before and after compression testing at the slowest strain rate. It is found in Fig. 7a that the upper part of the Cu NTs completely collapses with a mushroom deformation morphology. It seems that the Cu NTs with columnar grains (with average in-plane grain size $d \approx 40$ nm) split along GBs under compression. In contrast, the Cu NCs deform uniformly and exhibit significant barreling. Specifically, a series of multiple grain offsets are observed in the present Cu NCs (see Fig. 7b), similarly to $d \approx 60$ nm Ni NCs [58] and $d \approx 160$ nm Cu NCs [59]. Unlike the Cu nanostructured micropillars, all the present NL micropillars display the same deformation morphology, i.e. extrusion of soft Cu accompanied by barreling (see Fig. 7c–f). In general, soft-phase extrusion is unique to NL micropillars composed of soft and hard phases, and has been found in Al/SiC [60] and Al/Pd [61] after uniaxial compression. The deformation morphologies of all the present NL micropillars are $\dot{\varepsilon}$ independent within this limited data set.

Furthermore, we carried out additional FIB/SEM cross-sectional observations, from which one can clearly observe that it is the Cu squeezed out of the surface rather than the hard (X or Cu–Zr) phase, as shown in Fig. 7g and h for Cu/Zr NCNLs and Cu/Cu–Zr C/ANLs, respectively. Unexpectedly, some localized interfacial debonding regions are observed only in the Cu/X NCNLs compressed at a greater strain $\sim 30\%$ (see Fig. 7g), while the CCIs are still intact at a smaller strain $< 20\%$. It is found that the thickness of individual Cu layers is significantly reduced, while that of Zr thins slightly by ~ 5 – 10 nm. In contrast, no damage or debonding regions are observed at CAIs, implying that the interfacial slip contributes to the extrusion of soft Cu. As well as the crystalline Cu layers, the glassy Cu–Zr layers also thin remarkably, especially at the top of the small-tapered C/ANLs, without formation of shear bands (see Fig. 7h).

4. Discussion

4.1. Influence of sample fabrication on mechanical properties

To date, FIB milling is typically used to fabricate micro- and nanopillars to study small-scale plasticity and size effects in uniaxial compression [19,20]. However, FIB milling can introduce defects into the milled pillars by forming dislocation loops and surface amorphization [62,63]. Damage of this type is a known source of strengthening in bulk single crystals, implying that FIB-fabricated pillars may be stronger than bulk [62,63]. Therefore, as the relative surface area to volume ratio in pillars increases with decreasing pillar size, these ion damage effects become more adverse. Several recent findings have shown the opposite trend:

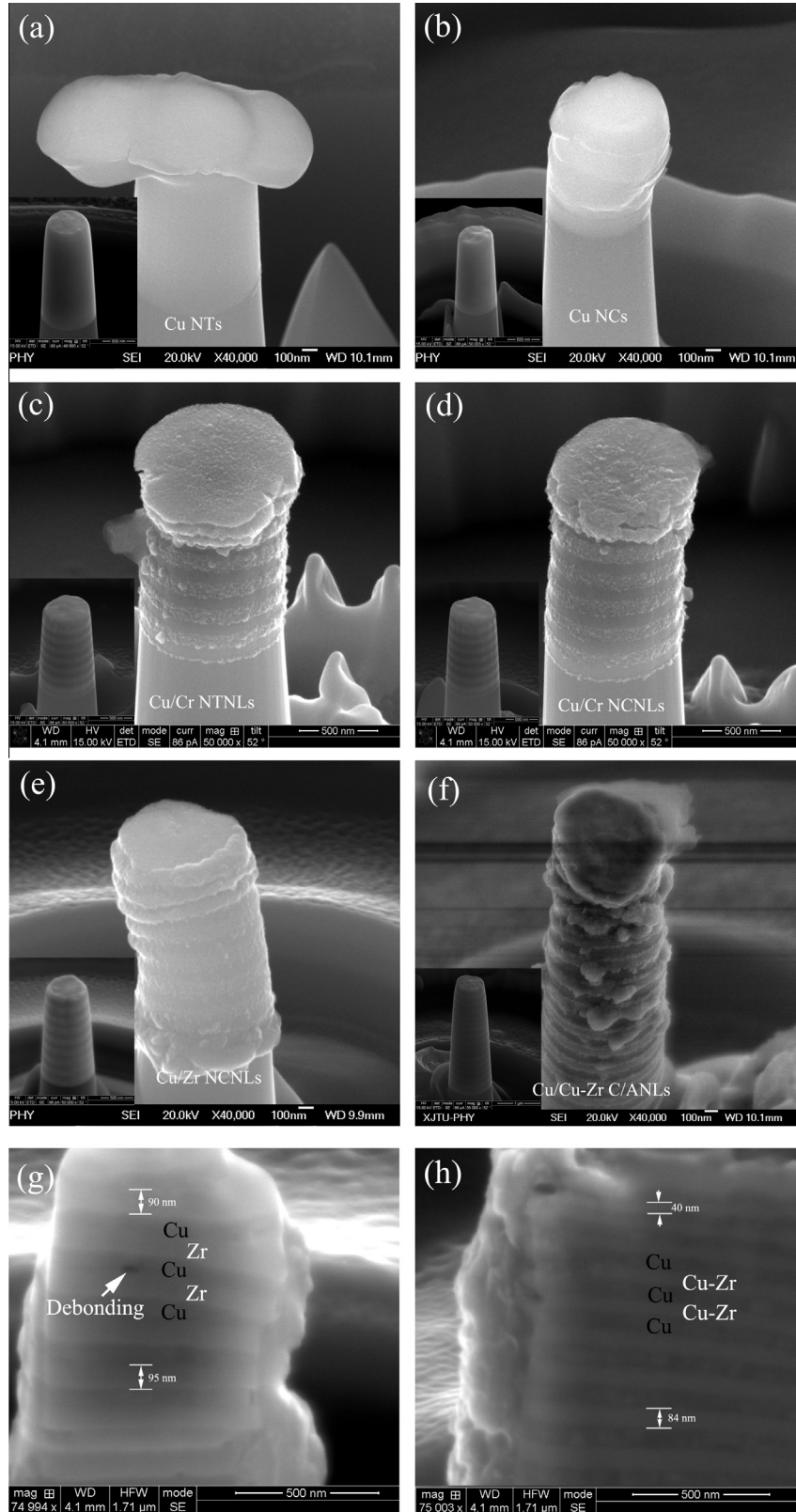


Fig. 7. Typical SEM images of (a) Cu NTs, (b) Cu NCs, (c) Cu/Cr NTNLS, (d) Cu/Cr NCNLS, (e) Cu/Zr NCNLS and (f) Cu/Cu-Zr C/ANLS after the uniaxial compression tests. Inset is the corresponding SEM image of the as-milled pillar. Typical cross-sectional FIB/SEM images (perpendicular to the interface planes) of the deformed (g) Cu/Zr NCNLS, showing the thinned Cu and Zr layers as well as the debonding region (indicated by an arrow), and (h) Cu/Cu-Zr C/ANLS, showing the significantly thinned Cu and Cu-Zr layers with intact CAIs.

FIB-free, pristine pillars yield at near-theoretical strength [64–66]. However, it has been shown that initially defect-free NiAl–Mo eutectic alloys undergo a significant decrease in strength after exposure to the FIB or pre-strain as a result of increasing damage/dislocation density [67]. Specifically, Jennings et al. [68] have pointed out that it is the initial dislocation density rather than the fabrication technique that drives the size effect in fcc metals [69–71]. This finding is consistent with previous work on body-centered cubic alloy systems [65–67], showing that the pillar strength is a strong function of the initial dislocation density.

In our experiments, the low beam current (15 pA) used in the fabrication process probably minimizes sample damage. Even though the same current (15 pA) was used, the Cu NCs are rougher than the Cu NTs (nanolayered pillars behave the same way). This result is most likely caused by the weaker resistance of GBs to Ga⁺ [72]. The roughness of the sample can lead to a broad variation in the initial stiffness of the material but does not significantly affect the strength [73,74]. Indeed, we have noticed that the slope of the loading curve is much smaller than that of unloading curve, and that the Cu/X NCNLs and Cu/Cu–Zr C/ANLs have similar strengths $\sigma_{0.5} \approx 1.5$ GPa. These results agree well with the measured hardness of the corresponding as-deposited multilayers (with the almost same hardness ~ 4.5 GPa [52,75]) and the extrusion of Cu in NL systems. Thus, the effects of FIB milling on the mechanical properties of all the samples are likely to act in a similar way, and their effects are not considered in the following discussion.

4.2. Intrinsic size- and strain-rate-dependent dislocation storage

The plastic deformation of crystals results from the nucleation and motion of dislocations on crystallographic planes. As the irreversible deformation proceeds, dislocations multiply and their mutual interactions hinder their motion, causing the metals to become strain hardened [76]. The strain-hardening behavior is closely linked to the size- and rate-dependent stored dislocation density (ρ) [76–78]. Considering the possible absorption of a dislocation by GBs (or interfaces) with the probability P_{dis} in nanostructures [77], ρ can be expressed as [54,78]:

$$\rho = \rho_0 + (1 - P_{\text{dis}})\rho_n = \rho_0 + (1 - P_{\text{dis}})\varepsilon_p/(bs), \quad (4)$$

where ρ_0 is the density of pre-existing dislocations and those introduced by FIB milling, roughly of the order of $\sim 10^{12}$ – 10^{14} m⁻², ρ_n is the density of newly generated dislocations during plastic deformation, s is the mean free path (the distance that dislocations travel before being frozen by the microstructure), and P_{dis} can be given by [54,78]:

$$P_{\text{dis}} = [1 - (1 - p)^N]^J = \left\{ 1 - \left[1 - \exp\left(\frac{-(\Delta G + \tau_0 b^3)}{k_B T}\right) \right]^{\frac{sbv}{\varepsilon d}} \right\}^{\omega l}, \quad (5)$$

where $p = \exp[-(\Delta G + \tau_0 b^3)/(k_B T)]$ is the probability of an atom successfully jumping into the GB in a single attempt; $N = (sbv)/(\varepsilon d)$ is the number of attempted jumps by dislocation core atoms to the GB interface during a given time; $J = \omega l$ is the total number of atoms on the dislocation core jumping into the GB, where the dislocation length l is proportional to d or h ; ΔG is the activation energy for atomic migration (or dislocation emission), which varies over the range ~ 0.6 – 0.95 eV [21,77], and is a decreasing function of the effective stress (or proportional to the characteristic size d or h) [79,80]; v is the Debye frequency; τ_0 is the resolved shear stress; ω physically corresponds to the atomic linear density of the dislocation core and is independent of d or h ; and other symbols have the same meaning as above.

By using $\Delta G = 0.8$ eV, $b = 0.2556$ nm, $v = 7.2 \times 10^{12}$ Hz, $T = 300$ K, $l = d$, $\tau_0 = s\sigma_0 = 41$ MPa [77], $\omega = 6.5$ atoms nm⁻¹ and Eq. (5), we find that the critical size for $P_{\text{dis}} = 0$ decreases from 30 to 5 nm as the strain rate increases from 2×10^{-4} to 2×10^{-3} s⁻¹. This implies that above the critical size the storage of dislocations within the lattice is preferred, but below this critical size the trap/absorption of dislocations by GBs (or interfaces) prevails [81,82]. Therefore, as the internal size is greater than ~ 30 nm, dislocations can accumulate in grain interiors, contributing to the hardening. It should be noted that this model does not consider the effects of dislocation pile-ups, more details of which can be found in Refs. [54,78].

4.3. Homogeneous TB/GB effects on the SRS of Cu nanostructures

4.3.1. Microstructures and TB/GB effects on the stress–strain response

Shifts in yield mechanisms generally result in corresponding shifts in deformation behaviors. The true stress–strain curves of the Cu NTs show the hardening–softening–hardening transition for the whole plastic region. However, the rapid, large stress drops in the stress–strain curves seen in the Cu NTs are completely absent in the curves of the Cu NCs, which only show the hardening–to-softening transition. This suggests that the deformation processes in the Cu NTs are very different from those of NCs. The small $V^* < 10b^3$ indicates that the dislocations are emitted from the GBs in the Cu nanostructures, including NTs and NCs, in agreement with the atomistic simulations [83]. The hardening behavior at the initial stage of plastic flow ($\varepsilon_p \leq 4\%$) can therefore be attributed to the accumulation of dislocations and their interactions with TBs/GBs [27,84,85]. For the intermediate strain range ($4\% < \varepsilon_p < 10\%$), sharp softening emerges in the Cu NTs. This phenomenon can be explained by considering the following two factors. First, and most importantly, the structural collapses of Cu NTs can induce sudden stress drops, due to the operation of GB-mediated processes. Secondly, detwinning likely occurs in Cu NTs with twin thickness $\lambda < 10$ nm, leading to stress drops [30,34,86]. The

subsequent dislocation–TB interactions can contribute to the enhanced strength at great plastic strains ($\varepsilon_p \geq 10\%$).

However, at large plastic strains, only the softening behavior is observed in the Cu NCs without great stress drops. This behavior in the Cu NCs can be rationalized in terms of the multicrystalline structure. That is to say, the number of grains across the diameter in this study is ~ 15 for the Cu NTs, while is ~ 5 for the Cu NCs. Due to the weak constraining effect of the free surface, the high external stress causes the GB-sliding process to be switched on in Cu NCs, which results in the formation of grain offsets (see Fig. 7b) [59,87]. Therefore, it is conceivable that the GB-mediated mechanisms contribute to the strength reduction in Cu NCs [58,88].

On the other hand, the SRS—the fact that materials harden faster at greater strain rates—is better represented by Orowan’s law [84]: $\dot{\varepsilon} \propto \rho b v$, where $\dot{\varepsilon}$ is the strain rate, ρ is the dislocation density, b is the Burgers vector and v is the average dislocation velocity. In this case, in addition to the dislocation storage, the dislocation velocity will become important. As mentioned above, the emitted and pre-existing dislocations can be stored within a grain with $d > 30$ nm at all strain rates used here, and a higher rate leads to more dislocations being stored [77,78]. This significantly enhances the stress level at a small plastic strain, as predicted from the famous Taylor’s hardening law [85]. In addition, the SRS is related to the spatiotemporal characteristics of crystal slip. In plastically deformed single crystals, internal dislocation avalanches can lead to successive jumps in the stress–strain curves (strain bursts) [89,90]. Nevertheless, in the present Cu nanostructures the strain-burst-related stress drops are effectively suppressed owing to the presence of GBs, especially at faster strain rates [54,90].

4.3.2. Normal strain-dependent SRS

In coarse-grained fcc metals (e.g. Cu) that strengthen via the well-defined forest dislocation hardening, the SRS usually changes with ε_p as the microstructural features (density or spacing of dislocations) evolve with the magnitude of plastic deformation [53,91]. Similarly, in the present nanomaterials, including Cu nanostructures and NL systems, the dislocation substructures may evolve with ε_p at different strain rates, supporting the strain-hardening behavior observed in the stress–strain curves. In other words, accumulation and interactions of dislocations (i.e. ordinary forest hardening) probably leads to the evolution of internal dislocation structures with ε_p [47,54,92], thereby altering SRS m (see Figs. 3 and 4) [26,53,91]. Here, the SRS of both Cu NCs and NTs increases with decreasing ε_p (defined as “normal” strain-dependent SRS), similarly to bulk NT Cu (with $\lambda \approx 15 \pm 7$ and $\lambda \approx 100 \pm 15$ nm, respectively) [56]. Lu and coworkers [28,29] have shown that the GBs and TBs play similar roles in the plastic deformation of Cu. Specifically, when the NC Cu and NT Cu have a similar internal feature size, e.g. $d = \lambda = 100$ nm, they exhibit nearly identical $m \approx 0.02$ [28,29]. Here, one can find

that as the sample sizes of the Cu nanostructures are reduced to ~ 550 nm, the m values of the Cu NCs are much larger than those of their bulk counterparts, in sharp contrast with the Cu NTs. This is probably caused by a smaller diameter-to-grain size ratio ~ 5 for the Cu NCs and a larger diameter-to-twin thickness ratio ~ 65 for the Cu NTs.

To elucidate this strain-dependent, rate-limiting behavior, we follow the thinking of Zerilli and Armstrong [53] by considering the length scales in NC grains during GB–dislocation interactions (called the GBD model hereinafter), similarly to Cheng et al. [93]. In the GBD model, SRS m can be related to an activation volume V^* of the thermally activated event as Eq. (3). For fcc metals, V^* can also be written as [53]:

$$V^* = b\chi l^*, \quad (6)$$

where b is the Burgers vector of the dislocations, χ is the distance (of the order of b) swept out by the mobile dislocation during one activation event, and l^* is the length of the dislocation segment involved in the thermal activation (or the Friedel sampling length that scales with the average contact distance between two obstacles). Combining Eqs. (3) and (6), we get:

$$m = \frac{\sqrt{3}k_B T}{\sigma V^*} = \frac{\sqrt{3}k_B T}{\sigma b\chi l^*}, \quad (7)$$

in which χ is approximately constant. On the other hand, the strength has contributions from not only the dislocations but also the GBs, and can be derived to be [93,94]:

$$\sigma = \sigma_0 + \alpha\sqrt{\rho} + \beta/\sqrt{d}, \quad (8)$$

where the first term accounts for the lattice friction, the second term arises from the Taylor equation, and the third term stems from the Hall–Petch relation. α and β are proportionality factors. The obstacle spacing l^* can be viewed as having two possible limits, l_1^* and l_2^* [93]:

$$l_1^* = \xi/\sqrt{\rho}, \quad (9a)$$

$$l_2^* = \zeta d, \quad (9b)$$

where ξ and ζ are proportionality factors. l_1^* is the controlling length scale when d and ρ are both large such that ρ plays the dominant role. Neglecting the very small lattice friction of fcc metals, SRS m can be expressed as:

$$m = \frac{\sqrt{3}k_B T}{b\chi} \frac{1}{\alpha\xi + \beta\xi/\sqrt{\rho d}}. \quad (10a)$$

Alternatively, l_2^* is the controlling length scale and is of the order of the length of a GB dislocation source or the spacing between the trapped dislocations and GBs in our deformed Cu nanostructures. We thus derive:

$$m = \frac{\sqrt{3}k_B T}{b\chi} \frac{1}{\zeta(\alpha\sqrt{\rho d} + \beta\sqrt{d})}. \quad (10b)$$

Taking $d = 110$ nm and $s \propto d$, we find that the m value calculated from Eq. (10b) changes markedly for Cu NTs and NCs at different strains. It agrees well with the present

results. On the other hand, V^* increases with increasing ε_p , but remains lower than $10b^3$. It is suggested that the deformation mechanisms of the present two Cu nanostructures do not change, i.e. multicrystalline Cu pillars deform via the operation of GB sources [26].

4.4. Heterophase interfaces effects on the SRS of Cu-based NL micropillars

4.4.1. Strain-rate effects on hardening/softening behavior

The true stress–strain curves for the samples of Cu/X NTNLS and NCNLS and Cu/Cu–Zr C/ANLS are nearly identical in every respect, showing a smooth transition from elastic to plastic deformation without any sharp stress drops. In nanoscaled multilayers, it is also the multiplication and interaction of dislocations that causes the materials to be less deformable. In the present experiments, a hardening-to-softening transition is observed in the NL systems at low $\dot{\varepsilon}$, but the softening behavior is strongly inhibited at high $\dot{\varepsilon}$. This is because at faster $\dot{\varepsilon}$ more dislocations interact with each other and/or with TBs/interfaces [78,81,82,95], which in turn retards the softening behavior. The hardening behavior can be ascribed to dislocation storage and dislocation–interface interactions, as discussed in Refs. [46,47,78,96,97]. In contrast, the possible mechanisms for the softening at low $\dot{\varepsilon}$ are as follows: (i) the annihilation of dislocations as well as the operation of GB-mediated processes can lead to softening [46,47,96,97]; and (ii) the detwinning process in the NTNLS likely results in losing the TB strengthening effect [30,34,86].

4.4.2. Inverse strain-dependent SRS

Previously, it was found that the SRS m of both Cu NTs and Cu NCs decreases with increasing ε_p . In sharp contrast with the Cu nanostructures, the SRS of all the Cu-based NL micropillars monotonically increases with increasing ε_p . Here, we refer to this unique phenomenon emerging in NL systems as the “inverse” strain effect to distinguish it from the “normal” strain effect observed in single-phase Cu nanostructures. In particular, the Cu/X NTNLS, in which the TBs and heterophase interfaces coexist, exhibit increased m with increasing ε_p . These observations suggest that it is the heterophase interfaces rather than the TBs/GBs that govern the rate-limiting processes in NL materials.

To elucidate the inverse strain-dependent SRS m , we still employ the GBD model to rationalize the experimental findings in NL micropillars. To begin, let us consider the internal features of NL materials. Physical explanations for increased SRS m (and decreased V^*) in NC fcc metals include the emission of partial/full dislocations within the nanometric constraint of a three-dimensional network of GBs/TBs [3,55]. This strong three-dimensional constraining effect can induce an explosive increase in ρ (i.e. dislocation avalanches), while s increases slightly at a greater plastic strain. This behavior is similar to that of passivated single-crystal pillars [98–100]. For nanoscaled multilayers, as in this study, the nanometer constraint is achieved in only

one dimension, with heterophase interfaces inducing highly anisotropic dislocation mobility [57,81], in the form of parallel (confined layer slip) vs. perpendicular (slip transmission or climb) motion. Theoretical calculations [82] have shown that in nanoscaled crystalline/crystalline multilayers, it is more favorable to deform a layer by a single dislocation (loops) of confined layer propagation on numerous planes rather multiple dislocations (loops) of confined layer propagation on fewer planes. It is suggested that a lower density of dislocations can achieve a greater plastic strain in multilayers than that in Cu nanostructures. In situ TEM observations in the stretched 30 nm Cu/60 nm Ni multilayers have shown that as the dislocations encounter the first boundary, they spread laterally within the layer until a source nucleates at the interface, bowing into the next layer [82]. Therefore, once a source operates in individual Cu layers, dislocations will be confined to Cu unless they can overcome the barriers of CCIs and propagate in adjacent X layers. However, if they do overcome the barriers, Cu layers on both sides of each X layer may inject dislocation loops into the X layer, leading to plastic deformation of the multilayer [82]. This implies that the mean free path s in NL samples is far greater than that in Cu nanostructures. Specifically, the deformation by uniform confined layer propagation in either compressive (and shear) or stretching mode is predicted to require a constant stress, $\eta\sigma_{\text{Com}} = \tau_{\text{She}} = \sigma_{\text{Str}} = \mu b \ln(h/b)/(2\pi h)$, for $\varepsilon_p \approx b/(10h)$, where η is a strain resolution factor for the active slip systems [82]. However, for $\varepsilon_p > b/(10h)$ single slip of confined layer propagation events begin to interact with the misfit dislocations net so that σ_{Com} or τ_{She} (mobile dislocation density) begins to decrease with plastic shear strain, but σ_{Str} (sessile dislocation density) begins to increase with plastic stretching strain [82]. The difference arises because the dislocation line energy behaves differently with s , depending on the compressing/shearing vs. stretching configuration. Therefore, at a greater plastic strain, ρ cannot continuously increase above a critical density on the order of $\sim 10^{16} \text{ m}^{-2}$ [81,101], or even decreases due to dislocation annihilation [101], in good agreement with the hardening-to-softening transition in the true stress–strain curves. Meanwhile, the mean free path of dislocations traveling in the interfaces can increase markedly. This is because the interfaces are easily sheared under the stress field of a lattice dislocation near the interface, and hence the sheared interface attracts and traps the dislocation within the interface, where the dislocation undergoes core spreading [95,102]. In this regard, ε_p is mainly dominated by s rather than ρ , i.e. the larger is ε_p the greater is s (or the lower is ρ). This creates an inverse strain effect on the SRS in Cu/X nanolayers, in good agreement with the prediction from Eq. (10) using $s \propto d \cdot (100 \cdot \varepsilon_p)^2$ (see the fitting curves in Fig. 5b).

4.4.3. Comparisons between CCIs and CAIs in NL micropillars

The high strength of multilayers essentially originates from the confined dislocation mobility within the

constituent layer channel, i.e. the blockage of the heterophase interfaces to dislocation pile-ups or single dislocations [44,52,75,82]. Thus, the interface characteristics undoubtedly play important roles in determining the strengths and deformation behaviors of multilayers. Recent findings [103,104] have shown that a higher strength is derived from the ability of the interfaces to trap dislocations through the relatively easier interfacial shear in NL materials, due to dislocation core spreading along the weak interfaces. This is consistent with the fact that the Cu/Cr nanolayer which has a lower interface shear strength exhibits a higher peak strength than the Cu/Zr nanolayer [48,52,75]. On the other hand, the interface strength is closely correlated with the interface misfit strain or the density of misfit dislocations, which contribute to the SRS of NL materials due to dislocation–interface (dislocation) interactions [1–6]. Therefore, in the Cu/X NCNLs, it is likely to find that the Cu/Zr exhibits higher m than Cu/Cr, despite the SRS m of Cr ≈ 0.012 being larger than that of Zr (≈ 0.003) at the same $h = 125$ nm with $d \approx 15$ nm [48].

In the present experiments, because the soft Cu layers mainly dominate the plastic flow, all the NL samples exhibit the same surface morphology, i.e. extrusion of Cu in between the hard layers, and the NCNLs and the C/ANLs exhibit almost identical strength, $\sigma_{0.5} \approx 1.5$ GPa. However, the internal deformation features of the NCNLs and the C/ANLs are quite different. The former shows localized interfacial debonding regions at great strains $\sim 30\%$, while the latter exhibits intact interfaces. Specifically, the nanoscaled glassy Cu–Zr layers exhibit homogeneous-like plasticity without shear banding, supporting the smooth compressive curves. In the crystalline/crystalline NL micropillars, slip/shear transfer happens by either core spreading along the shear–weak interface or triggering of new slips in the companion grain but only at very limited selections of Burgers vectors and slip planes near CCIs (or GBs) [42,104]. Thus, large incompatibility and stress concentrations could build up inside or near the CCIs (or GBs) during deformation, leading to interfacial debonding. Additionally, this can result in asymmetric slip events and cause shear along CCIs, resulting in the shear failure of crystalline/crystalline micropillars, as is verified in Cu/Nb [103] and Cu/Zr [47,96] NL micropillars at small $h \leq 50$ nm. Atomistic simulations [95] and in situ TEM observations [81,82] have demonstrated a much higher dislocation density at the interface as compared with the bulk, indicating preferential trapping of dislocations at the interfaces during deformation of nanolayers, similarly to the NT metals [28].

In the C/ANLs, the glassy layers act as high-capacity sinks for dislocations, enabling the absorption/annihilation of dislocations emitted from CAIs [42,105–107], which in turn affects their mechanical response. For example, the present authors have found the hardness of crystalline/amorphous Cu/Cu–Zr multilayers to be greater than that of crystalline/crystalline Cu/Zr multilayers at small $h = 5$ nm, above which both of them have identical hardness at a given h [52]. Unlike the CCIs, the CAIs exhibit

some unique features of shear/slip transfer [42,105]. Such an “extreme incompatibility” scenario will seldom arise at the CAIs, because the shear transition zones in the amorphous materials are omnidirectional, i.e. there are infinite selections of possible inelastic shear modes to transfer to [42]. In this regard, the C/ANLs exhibit homogeneous-like deformation rather than localized interfacial debonding, as verified in Cu/Cu–Zr [46,108] and Cu/PdSi [109] nanolayers. Our further experimental findings have shown that the glassy Cu–Zr layers are crystallized as the Cu/Cu–Zr C/ANLs are compressed to $\sim 30\%$ strain, which is most likely linked to the absorption of dislocations by glassy layers. The amorphous-to-crystalline transition has been discussed elsewhere [110] and is beyond the scope of the present work.

5. Conclusions

By employing microcompression methodology, we systematically studied the plastic deformation of Cu NTs and NCs, Cu/X NTNLS and NCNLs, and Cu/Cu–Zr C/ANLs at similar sample dimensions but different strain rates to reveal the fundamental differences between homogeneous boundaries (GBs and TBs) and heterophase interfaces (CCIs and CAIs) and their coupling effects in small-scale plasticity. The main findings are summarized as follows:

- (1) Faster strain rates effectively enhance the hardening of Cu nanostructures and NL nanomaterials, due to more dislocations being stored. The Cu nanostructures with homogeneous boundaries exhibit a normal strain effect on SRS, while the Cu-based NL micropillars with heterophase interfaces exhibit an inverse strain effect on SRS, both of which are quantitatively explained by a dislocation mode by considering the microstructure-constraining effects on the mean free path of dislocations.
- (2) Although Cu-based NCNLs exhibit much lower flow stresses and SRS than the corresponding NTNLS, their SRS is mainly controlled by the interfaces and is strongly influenced by the interfacial characteristics, e.g. misfit strains.
- (3) Due to the strain incompatibility near the CCIs, the crystalline/crystalline NL materials exhibit localized interfacial debonding in plastic deformation. In contrast, the CAIs exhibit unique shear/slip transfer characteristics, making the C/ANLs prone to deform homogeneously via interfacial slip.

Acknowledgements

This work was supported by the National Natural Science Foundation of China (Grant Nos. 50971097, 51201123), the 973 Program of China (Grant No. 2010CB631003), and the 111 Project of China (B06025).

G.L. is grateful for support from Fundamental Research Funds for the Central Universities and the Tengfei Scholar project. J.Y.Z. thanks the China Postdoctoral Science Foundation some financial support (2012M521765). Access to the nanoindentation equipments in CAMP-Nano is also acknowledged. The authors greatly appreciate the valuable suggestions/comments of the reviewer.

References

- [1] Arzt E. *Acta Mater* 1998;46:5611–26.
- [2] Meyers MA, Mishra A, Benson DJ. *Prog Mater Sci* 2006;51:427–556.
- [3] Dao M, Lu L, Asaro RJ, De Hosson JTM, Ma E. *Acta Mater* 2007;55:4041–65.
- [4] Kumar KS, Van Swygenhoven H, Suresh S. *Acta Mater* 2003;51:5743–74.
- [5] Zhu T, Li J. *Prog Mater Sci* 2010;55:710–57.
- [6] Arzt E, Dehm G, Gumbsch P, Kraft O, Weiss D. *Prog Mater Sci* 2001;46:283–307.
- [7] Pande CS, Cooper KP. *Prog Mater Sci* 2009;54:689–706.
- [8] Shan ZW, Mishra RK, Asif SAS, Warren OL, Minor AM. *Nat Mater* 2008;7:115–9.
- [9] Greer JR, Nix WD. *Phys Rev B* 2006;73:245410–.
- [10] Chisholm C, Bei H, Lowry MB, Oh J, Syed Asif SA, Warren OL, et al. *Acta Mater* 2012;60:2258–64.
- [11] Huang L, Li QJ, Shan ZW, Li J, Sun J, Ma E. *Nat Commun* 2011;2:547.
- [12] Zhou C, Beyerlein IJ, LeSar R. *Acta Mater* 2011;59:7673–82.
- [13] Chen J, Lu L, Lu K. *Scripta Mater* 2006;54:1913–8.
- [14] Schwaiger R, Moser B, Dao M, Chollacoop N, Suresh S. *Acta Mater* 2003;51:5159–72.
- [15] Hirakata H, Fukuhara N, Ajioka S, Yonezu A, Sakihara M, Minoshima K. *Acta Mater* 2012;60:4438–47.
- [16] Karanjgaokar NJ, Oh CS, Lambros J, Chasiotis I. *Acta Mater* 2012;60:5352–61.
- [17] Greer JR, De Hosson JTM. *Prog Mater Sci* 2011;56:654–724.
- [18] Dehm G. *Prog Mater Sci* 2009;54:664–88.
- [19] Kraft O, Gruber PA, Mönig R, Weygand D. *Annu Rev Mater Res* 2010;40:293–317.
- [20] Uchic MD, Shade PA, Dimiduk DM. *Annu Rev Mater Res* 2009;39:361–86.
- [21] Jennings AT, Li J, Greer JR. *Acta Mater* 2011;59:5627–37.
- [22] Schneider AS, Clark BG, Frick CP, Gruber PA, Arzt E. *Mater Sci Eng A* 2009;508:241–6.
- [23] Momprou F, Legros M, Sedlmayr A, Gianola DS, Caillard D, Kraft O. *Acta Mater* 2012;60:977–83.
- [24] Rao SI, Dimiduka DM, Tang M, Uchic MD, Parthasarathy TA, Woodward C. *Philos Mag* 2007;87:4777–94.
- [25] Oh SH, Legros M, Kiener D, Dehm G. *Nat Mater* 2009;8:95–100.
- [26] Zhu T, Li J, Samanta A, Leach A, Gall K. *Phys Rev Lett* 2008;100:025502.
- [27] Christian JW, Mahajan S. *Prog Mater Sci* 1995;39:1–157.
- [28] Lu L, Chen X, Huang X, Lu K. *Science* 2009;323:607–10.
- [29] Lu L, Zhu T, Shen Y, Dao M, Lu K, Suresh S. *Acta Mater* 2009;57:5165–73.
- [30] Jang D, Li X, Gao H, Greer JR. *Nat Nano* 2012;7:594–601.
- [31] Wu ZX, Zhang YW, Srolovitz DJ. *Acta Mater* 2009;57:4508–18.
- [32] Wu ZX, Zhang YW, Srolovitz DJ. *Acta Mater* 2011;59:6890–900.
- [33] Lu L, You ZS, Lu K. *Scripta Mater* 2012;66:837–42.
- [34] Wang J, Li N, Anderoglu O, Zhang X, Misra A, Huang JY, et al. *Acta Mater* 2010;58:2262–70.
- [35] Brons JG, Padilla Ii HA, Thompson GB, Boyce BL. *Scripta Mater*.
- [36] Chen Y, Liu Y, Sun C, Yu KY, Song M, Wang H, et al. *Acta Mater* 2012;60:6312–21.
- [37] Liu Y, Bufford D, Wang H, Sun C, Zhang X. *Acta Mater* 2011;59:1924–33.
- [38] Zhang X, Misra A, Wang H, Shen TD, Nastasi M, Mitchell TE, et al. *Acta Mater* 2004;52:995–1002.
- [39] Zhang JY, Zhang X, Wang RH, Lei SY, Zhang P, Niu JJ, et al. *Acta Mater* 2011;59:7368–79.
- [40] Zhang JY, Liu G, Zhang X, Zhang GJ, Sun J, Ma E. *Scripta Mater* 2010;62:333–6.
- [41] Kim JY, Jang DC, Greer JR. *Adv Funct Mater* 2011;21:4550–4.
- [42] Wang YM, Li J, Hamza AV, Barbee JTW. *Proc Natl Acad Sci USA* 2007;104:11155–60.
- [43] Was GS, Foecke T. *Thin Solid Films* 1996;286:1–31.
- [44] Misra A, Hirth JP, Hoagland RG. *Acta Mater* 2005;53:4817–24.
- [45] Bhattacharyya D, Mara NA, Dickerson P, Hoagland RG, Misra A. *Acta Mater* 2011;59:3804–16.
- [46] Zhang JY, Liu G, Lei SY, Niu JJ, Sun J. *Acta Mater* 2012;60:7183–96.
- [47] Zhang JY, Lei S, Niu J, Liu Y, Liu G, Zhang X, et al. *Acta Mater* 2012;60:4054–64.
- [48] Niu JJ, Zhang JY, Liu G, Zhang P, Lei SY, Zhang GJ, et al. *Acta Mater* 2012;60:3677–89.
- [49] Greer JR, Oliver WC, Nix WD. *Acta Mater* 2005;53:1821–30.
- [50] Bharathula A, Lee SW, Wright WJ, Flores KM. *Acta Mater* 2010;58:5789–96.
- [51] Lee S-W, Han SM, Nix WD. *Acta Mater* 2009;57:4404–15.
- [52] Zhang JY, Liu Y, Chen J, Chen Y, Liu G, Zhang X, et al. *Mater Sci Eng A* 2012;552:392–8.
- [53] Zerilli FJ, Armstrong RW. *J Appl Phys* 1987;61:1816.
- [54] Zhang JY, Liu G, Sun J. *Int J Plast* 2013. <http://dx.doi.org/10.1016/j.ijplas.2013.03.009>.
- [55] Gu P, Dao M, Asaro RJ, Suresh S. *Acta Mater* 2011;59:6861–8.
- [56] Shen YF, Lu L, Dao M, Suresh S. *Scripta Mater* 2006;55:319–22.
- [57] Carpenter JS, Misra A, Uchic MD, Anderson PM. *Appl Phys Lett* 2012;101:051901.
- [58] Jang D, Greer JR. *Scripta Mater* 2011;64:77–80.
- [59] Jang DC, Cai C, Greer JR. *Nano Lett* 2011;11:1743–6.
- [60] Singh DRP, Chawla N, Tang G, Shen YL. *Acta Mater* 2010;58:6628–36.
- [61] Dayal P, Quadir MZ, Kong C, Savvides N, Hoffman M. *Thin Solid Films* 2011;519:3213–20.
- [62] Kiener D, Motz C, Rester M, Jenko M, Dehm G. *Mater Sci Eng A* 2007;459:262–72.
- [63] Mayer J, Giannuzzi LA, Kamino T, Michael J. *MRS Bull* 2007;32:400.
- [64] Richter G, Hillerich K, Gianola DS, Monig R, Kraft O, Volkert CA. *Nano Lett* 2009;9:3048–52.
- [65] Bei H, Shim S, George EP, Miller MK, Herbert EG, Pharr GM. *Scripta Mater* 2007;57:397–400.
- [66] Bei H, Shim S, Pharr GM, George EP. *Acta Mater* 2008;56:4762–70.
- [67] Shim S, Bei H, Miller MK, Pharr GM, George EP. *Acta Mater* 2009;57:503–10.
- [68] Jennings AT, Burek MJ, Greer JR. *Phys Rev Lett* 2010;104:135503.
- [69] El-Awady JA, Uchic MD, Shade PA, Kim S-L, Rao SI, Dimiduk DM, et al. *Scripta Mater* 2013;68:207–10.
- [70] Schneider AS, Kiener D, Yakacki CM, Maier HJ, Gruber PA, Tamura N, et al. *Mater Sci Eng A* 2013;559:147–58.
- [71] Rao SI, Dimiduk DM, Parthasarathy TA, Uchic MD, Tang M, Woodward C. *Acta Mater* 2008;56:3245–59.
- [72] Han WZ, Demkowicz MJ, Fu EG, Wang YQ, Misra A. *Acta Mater* 2012;60:6341–51.
- [73] Kiener D, Grosinger W, Dehm G, Pippan R. *Acta Mater* 2008;56:580–92.
- [74] Kiener D, Minor AM. *Acta Mater* 2011;59:1328–37.
- [75] Misra A, Verdier M, Lu YC, Kung H, Mitchell TE, Nastasi M, et al. *Scripta Mater* 1998;39:555–60.
- [76] Kocks UF, Mecking H. *Prog Mater Sci* 2003;48:171–273.
- [77] Carlton CE, Ferreira PJ. *Acta Mater* 2007;55:3749–56.

- [78] Lei SY, Zhang JY, Niu JJ, Liu G, Zhang X, Sun J. *Scripta Mater* 2012;66:706–9.
- [79] Jiang Q, Zhang SH, Li JC. *Solid State Commun* 2004;130:581–4.
- [80] Conrad H. *Mater Sci Eng A* 2003;341:216–28.
- [81] Li N, Wang J, Huang JY, Misra A, Zhang X. *Scripta Mater* 2010;63:363–6.
- [82] Anderson PM, Foecke T, Hazzledine PM. *MRS Bull* 1999;24:27–33.
- [83] Wu ZX, Zhang YW, Jhon MH, Greer JR, Srolovitz DJ. *Acta Mater*. [84] El-Azab A. *Science* 2008;320:1729–30.
- [85] Devincre B, Hoc T, Kubin L. *Science* 2008;320:1745–8.
- [86] Wang YM, FS, LaGrange T, Ott RT, Marian J, Barbee Jr TW, et al. *Nat Mater* 2013.
- [87] Gu XW, Loynachan CN, Wu Z, Zhang YW, Srolovitz DJ, Greer JR. *Nano Lett* 2012;12:6385–92.
- [88] Zhang JY, Cui JC, Liu G, Sun J. *Scripta Mater* 2013;68:639–42.
- [89] Dimiduk DM, Woodward C, Lesar R, Uchic MD. *Science* 2006;312:1188–90.
- [90] Csikor FF, Motz C, Weygand D, Zaiser M, Zapperi S. *Science* 2007;318:251–4.
- [91] Meyers MA. *Dynamic behavior of materials*. New York: John Wiley; 1994.
- [92] Frick CP, Clark BG, Orso S, Schneider AS, Arzt E. *Mater Sci Eng A* 2008;489:319–29.
- [93] Cheng S, Ma E, Wang YM, Kecskes LJ, Youssef KM, Koch CC, et al. *Acta Mater* 2005;53:1521–33.
- [94] Wei Q, Cheng S, Ramesh KT, Ma E. *Mater Sci Eng A* 2004;381:71–9.
- [95] Wang J, Misra A. *Curr Opin Solid State Mater Sci* 2011;15:20–8.
- [96] Zhang JY, Lei SY, Liu Y, Niu JJ, Chen Y, Liu G, et al. *Acta Mater* 2012;60:1610–22.
- [97] Misra A, Zhang X, Hammon D, Hoagland RG. *Acta Mater* 2005;53:221–6.
- [98] Jennings AT, Gross C, Greer F, Aitken ZH, Lee S-W, Weinberger CR, et al. *Acta Mater* 2012;60:3444–55.
- [99] El-Awady JA, Rao SI, Woodward C, Dimiduk DM, Uchic MD. *Int J Plast* 2011;27:372–87.
- [100] Ng KS, Ngan AHW. *Acta Mater* 2009;57:4902–10.
- [101] Nyilas K, Misra A, Ungár T. *Acta Mater* 2006;54:751–5.
- [102] Wang J, Misra A, Hoagland RG, Hirth JP. *Acta Mater* 2012;60:1503–13.
- [103] Mara NA, Bhattacharyya D, Hirth JP, Dickerson P, Misra A. *Appl Phys Lett* 2010;97:021909.
- [104] Hoagland RG, Kurtz RJ, Henager CH. *Scripta Mater* 2004;50:775–9.
- [105] Arman B, Brandl C, Luo SN, Germann TC, Misra A, Cagin T. *J Appl Phys* 2011;110:043539.
- [106] Legros M, Hemker KJ, Gouldstone A, Suresh S, Keller-Flaig RM, Arzt E. *Acta Mater* 2002;50:3435–52.
- [107] Hartmaier A, Buehler MJ, Gao HJ. *Mater Sci Eng A* 2005;400–401:260–2263.
- [108] Liu MC, Du XH, Lin IC, Pei HJ, Huang JC. *Intermetallics* 2012;30:30–4.
- [109] Knorr I, Cordero NM, Lilleodden ET, Volkert CA. *Acta Mater* 2013;61:4984–95.
- [110] Zhang JY, Liu G, Sun J. *Sci Rep* 2013;3:2324. <http://dx.doi.org/10.1038/srep02324>.